Unitary photoassociation: One-step production of ground-state bound molecules

S. Kallush and R. Kosloff

The Fritz Haber Research Center, The Hebrew University of Jerusalem, Jerusalem 91904, Israel
(Received 6 December 2007; published 29 February 2008)

Bound-state molecules can be photoassociated directly from ultracold free-atom pairs by excitation to a purely repulsive electronic state. The process is explained on the basis of quantum unitarity: the initially free-scattering state is transformed by an impulsive light pulse to a deformed superposition which contains bound-state components. For pulse durations which are short compared to the ultracold dynamics, the maximal rate of photoassociation was found to be determined by the initial stationary distribution of scattering states of the atom pairs. The process was simulated for an ultracold gas of ^{87}Rb with a temperature of $T=44$ μK and a density of $\approx 10^{11}$ cm^{-3}. Transform-limited pulses maximize the photoassociation, yielding ~ 1 bound molecule per pulse. Coherent control calculated by a local control scheme can increase the photoassociation yield by two orders of magnitude.

I. INTRODUCTION

Photoassociation (PA) is currently one of the most effective techniques for producing ultracold molecules. Both homonuclear and heteronuclear diatomic molecules have been assembled from atoms [1–4]. A typical experiment employs a narrow-band laser to promote free-scattering states into a bound molecular excited state. A second step transforms these excited bound-state molecules to bound states on the ground electronic surface. Recently, pulsed photoassociation has become a subject of interest, both experimentally [5,6] and theoretically [7–12]. The well-characterized initial condition in PA promoted the study of coherent control methods to enhance the PA rate [13–15].

The common conceptual framework used to explain the mechanism of photoassociation is based on perturbation analysis. The concept is to use a Feynman-like diagram to draw a sequence of first-order paths that lead from the initial to the final state (see the upper panel of Fig. 1). The initial state for photoassociation starts from a scattering state on the ground electronic surface. Hence, to first order, the transition dipole promotes part of this wave function to the excited electronic surface. In addition, the initial state stays intact. A second light-matter interaction transforms populating to bound molecular states on the ground electronic surface.

The drawback of perturbation theory is that it is nonunitary. Consequently, the initial state is assumed erroneously to remain unchanged during the process and the back action is ignored. Unitary perturbation theory corrects this problem, but it is rarely used. Diagrammatic perturbation theory is the source of a very useful language which supplies intuitive understanding of light-matter interactions. New concepts need to be developed which are consistent with the unitary principle.

The present paper demonstrates that for photoassociation the unitarity effect is important and can give rise to a mechanism for creating a significant number of bound molecules on the ground electronic state. The paper is organized as follows: The formal analysis of the process is presented in Sec. II. Section III describes the basic results for a Rb$_2$ sys-

tem showing the transition from the impulsive to the dynamic PA conditions. In Sec. IV a local control method is employed to optimize the unitarity effect for the dynamical case. Section V contains a deeper insight into the mechanism of the unitary PA and supplies an interpretation of the results of Sec. IV. Section VI summarizes and concludes the discussion.
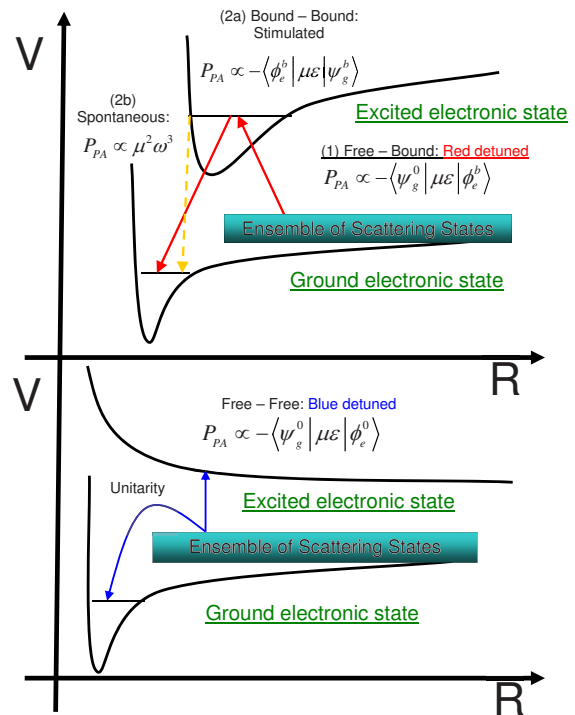
FIG. 1. (Color online) Two versions of photoassociation. Upper panel: two-step PA. Step 1: a red-detuned laser couples an ensemble of scattering states from the ground electronic surface to a bound state on the excited electronic surface. Step 2: a transfer of population from the electronic excited state to a bound ground vibration state via stimulated or spontaneous emission. Lower panel: one-step PA. A blue-detuned light removes amplitude from the ensemble of the ground electronic state. The remaining ensemble contains bound components by quantum unitarity.

II. PHOTOASSOCIATION MODEL

The Hilbert space of a photoassociation event is composed of a direct product of the internuclear degree of freedom, R, and the electronic degree of freedom. The center-of-mass motion can be omitted from this description. For sufficiently low temperatures only S-wave encounters are considered. The minimal model includes two electronic surfaces: a ground surface supporting both bound and free states and a purely repulsive excited surface supporting only scattering states.

For detuning values at the order of several cm^{-1} from the atomic resonance, the Condon radius is small enough and the electronic potentials are well separated energetically so that the two-states assumption is justified. Within the semiclassical description of the electromagnetic field, the Hamiltonian modeling the process has the form

$$\hat{\mathbf{H}} = \hat{\mathbf{H}}_0 + \hat{\mu} \cdot \tilde{\epsilon}(t), \tag{1}$$

where $\hat{\mathbf{H}}_0$ is the time-independent molecular Hamiltonian described in a diabatic framework, $\hat{\mu}$ is the electronic transition dipole moment operator, and $\tilde{\epsilon}$ is the external field. The total Hamiltonian, under the rotating-wave approximation, is thus

$$\hat{\mathbf{H}} = \begin{pmatrix} \dfrac{\hat{\mathbf{P}}^2}{2m} + \hat{\mathbf{V}}_g & -\mu \cdot \epsilon \\ -\mu \cdot \epsilon^\star & \dfrac{\hat{\mathbf{P}}^2}{2m} + \hat{\mathbf{V}}_e + \Delta \end{pmatrix}, \tag{2}$$

where $\frac{\hat{\mathbf{P}}^2}{2m}$ is the nuclear kinetic energy, m the reduced mass of the colliding partners, and $\hat{\mathbf{V}}_{g/e}(R)$ is the ground (excited) electronic potential energy surface. In this description $\epsilon(t)$ is the slowly varying envelope of the time-dependent external field and Δ is the detuning of the light from the atomic resonance. A dressed-state picture is used throughout this paper. The time duration of the process is shorter than the spontaneous emission lifetime (~ 20 ns); therefore, the dynamics can be considered as coherent. The ground-state $a\,^3\Sigma_u^+$ potential for the Rb$_2$ is identical to that in Ref. [12]. The repulsive wall of the potential is slightly adjusted to generate the measured scattering length of ^{87}Rb$_2$. The repulsive excited electronic state potential is taken from Ref. [16].

The dynamics was followed by solving the time-dependent Schrödinger equation. A mapped Fourier-grid method was used to represent the wave function [17,18]. A relative coordinate box of 9500 bohrs was represented. The initial state in all calculations was chosen as a stationary scattering state of the ground potential with energy corresponding to $E_0 = 44$ μK. This state was obtained by a numerical diagonalization of the stationary Hamiltonian with a mapped Fourier grid [18,19].

The photoassociation yield of bound-state molecules is defined by the expectation value of the projection operator $\hat{\mathcal{P}}_g = \hat{\mathbf{I}} \otimes |g\rangle\langle g|$:

$$\langle \hat{\mathcal{P}}_g \rangle = \langle \psi_g | \left(\sum_k |\phi_k\rangle\langle\phi_k| \right) | \psi_g \rangle, \tag{3}$$

where $|\psi_g\rangle$ is the instantaneous wave function for the ground electronic state and $\{|\phi_k\rangle\}$ is the complete set of bound states of the ground electronic potential. Practically, in all the examples presented in this paper only the last bound vibrational state is significantly populated, designated by ϕ. Under this assumption the summation in Eq. (3) is removed, leading to $\hat{\mathcal{P}}_g = |\phi\rangle\langle\phi| \otimes |g\rangle\langle g|$:

$$\langle \hat{\mathcal{P}}_g \rangle \approx |\langle \psi_g | \phi \rangle|^2 \equiv p_g^2, \tag{4}$$

where p_g^2 is the magnitude of the projection of the instantaneous ground-state wave function on the target wave function ϕ. This quantity measures the PA efficiency.

As was shown in [12], for ultracold collisions the total number of photoassociated molecules produced per pulse, $\mathcal{N}$, can be calculated from a single calculation starting from a scattering initial state and weighting the yield by a thermal factor:

$$\mathcal{N} = \sqrt{\frac{\pi}{2E_0}(k_B T)^3} \frac{N^2 \langle \hat{\mathcal{P}}_g(E_0) \rangle}{2Z\left[\frac{dE}{dn}\right]_{E_0}}. \tag{5}$$

Here, E_0 is the energy of the scattering state, T is the temperature, N is the number of atoms at the sample, and $\left[\frac{dE}{dn}\right]_{E_0}$ is the density of energy states evaluated at E_0, which could be approximated numerically as $\left[\frac{dE}{dn}\right]_{E_0} \approx E_{n+1} - E_n$. $\langle \hat{\mathcal{P}}_g(E_0) \rangle$ is the boxed-normalized quantity that was calculated by the single-scattering-state simulation, and Z is the partition function which is approximated classically for an ensemble of N noninteracting particles as

$$Z = V\left(\frac{mk_B T}{2\pi\hbar^2}\right)^{3/2} = \frac{V}{\Lambda^3}, \tag{6}$$

where Λ is the thermal de Broglie wavelength. Combining Eqs. (5) and (6) gives

$$\mathcal{N} = \frac{\pi^2 \hbar^3 N^2 \langle \hat{\mathcal{P}}_g(E_0) \rangle}{\sqrt{m^3 E_0} V\left[\frac{dE}{dn}\right]_{E_0}}. \tag{7}$$

In the present study, the conditions of the sample are assumed to be similar to those of the magneto-optical trap (MOT) in Ref. [6], with density $N/V \approx 10^{11}$ cm^{-3} and $N = 1.5 \times 10^5$. For the box size and scattering state energy taken here, $\left[\frac{dE}{dn}\right]_{E_0} = 6.3$ μK, and

$$\mathcal{N} = 3.8 \times 10^3 \langle \hat{\mathcal{P}}_g(E_0) \rangle = 3.8 \times 10^3 p_g^2. \tag{8}$$

This quantity is an estimate of the number of molecules that are produced per pulse. To compare to experiment, this value has to be multiplied by the repetition rate of the pulsed laser. Under Bose-Einstein condensate (BEC) conditions the initial density increases by about three orders of magnitude, while the number of atoms is reduced by an order of magnitude, so that the total yield can increase by roughly two orders of magnitude.
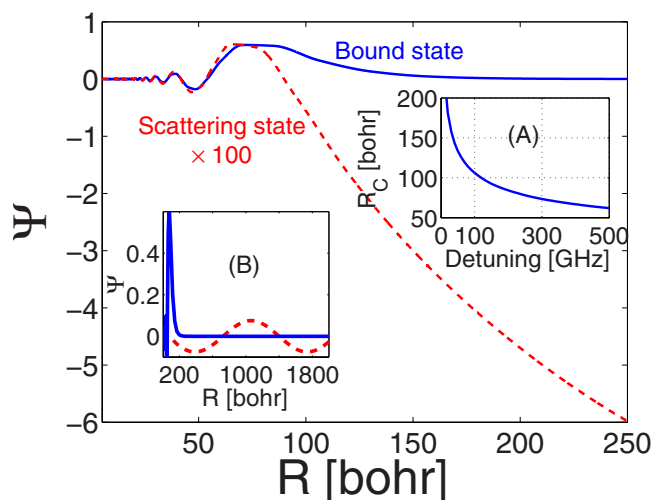
FIG. 2. (Color online) Principles of the unitary PA. The Rb_2 example. Main frame: a close-up view of the last bound-state wave function (solid blue line) and a scattering state (dashed red line, multiplied by a factor of 100 with respect to the box-normalized wave function). The similar nodal structure for $R < 100$ is obvious. Inset A: the Condon radius R_C as a function of the blue detuning from the S-P asymptote. Inset B: a larger view of the main frame.

III. RESULTS AND ANALYSIS

The unitarity photoassociation scheme is demonstrated by a blue-detuned excitation which can couple the ground potential only to a repulsive excited-state potential curve. Such an excited potential cannot support bound states. As a result, free–to–bound-state transitions can only take place on the *ground* electronic state. This is in contrast to pump-dump photoassociation schemes which employ frequencies *red detuned* from the atomic transition. Such frequencies induce a free–to–bound-state transition from the ground electronic state to a bound states on the excited electronic state. The second dump pulse further transforms this amplitude to bound states on the ground electronic surface.

A. Optimization of the pulse parameters: Detuning

The basic idea is that a single pulse is sufficient to induce photoassociation. The shortest blue-detuned pulse is studied first. This pulse is transform limited, characterized by the central frequency blue detuning from the atomic line and bandwidth which is inversely proportional to the pulse duration. Insight into the mechanism of the unitary photoassociation can be gained by noticing the similarities between the initial threshold scattering wave function and the last bound level. The nodal patterns in the region of the attractive part of the potential are identical. The two wave functions start to diverge for larger internuclear distances on the order of the scattering length. Figure 2 demonstrates these features for the Rb_2 example. The wave functions of the last bound state and a scattering state are shown. The scattering wave function is multiplied by a constant factor since the two wave functions are normalized differently. For the Rb system the similarities of nodal structure are found for distances less than $R < 100$ bohrs.
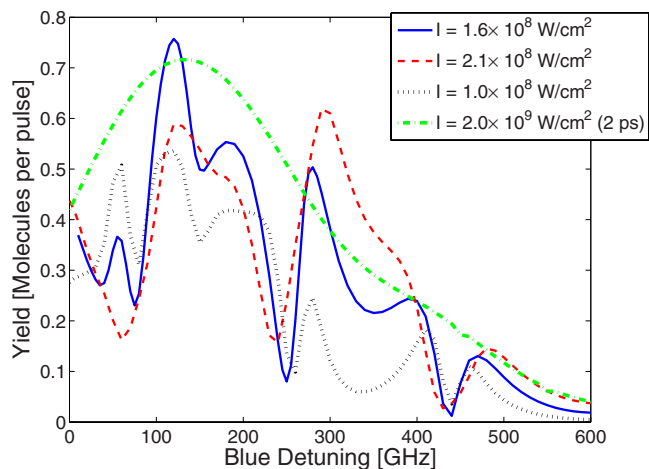
FIG. 3. (Color online) The PA yield as a function of detuning. The modulated lines represent three peak intensities of excitation by a transform-limited pulse with a pulse width of 15 ps. The dot-dashed green line represents the yield for a pulse width of 2 ps within the impulsive limit.

The unitary mechanism removes the amplitude of the scattering wave function at distances exceeding the scattering length. As a result, the inner part of the scattering wave function will transform to a bound state. Inset (A) of Fig. 2 presents the Condon radius as a function of the laser detuning from the atomic S-P resonance. The Condon point represents the point of resonance in the dressed-state picture between the ground- and excited-state potentials. In the impulsive limit most population transfer will take place in the vicinity of this point. For example, blue detuning of $\Delta \sim 120$ GHz will lead to a depletion of the amplitude of the ground-state wave function around $R \sim 100$ bohrs.

Figure 3 presents the bound-state yield $\mathcal{N}$ as a function of the laser detuning for four different intensities. The shortest pulse with a duration of 2 ps (green dashed line) shows a clear maximum at $\Delta = 120$ GHz. For this short time scale the process is impulsive; i.e., the nuclear dynamics is frozen both in *momentum* and in *position*. For longer pulses shown by three Gaussian profile pulses with a temporal width of 15 ps, a structure appears depending on the intensity of the pulse. These pulses are short relative to the ultracold spatial dynamics on the ground potential surface, but not with respect to the accumulation of momentum during the pulse. For all three intensities a maximum of the yield appears at $\Delta = 120$ GHz, as expected. These pulses display a violation of the Condon approximation, generating the structure that appears in Fig. 3. For the rest of this paper, the blue detuning is set to $\Delta = 120$ GHz.

B. Photoassociation yield vs intensity and temporal width

The dependence of the photoassociation yield on the pulse intensity and pulse duration is examined next. The main frame of Fig. 4 presents the PA yield versus the peak intensity of the pulse for a pulse width of 15 ps. The PA yield rises linearly with the field intensity, as expected from a first-order process—i.e., a removal of amplitude from the ground-state
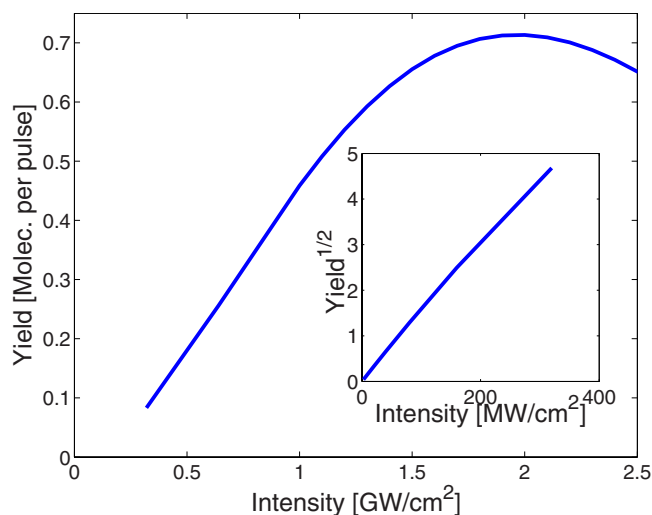
FIG. 4. (Color online) Main frame: the photoassociation yield as a function of intensity. The pulse has a Gaussian shape with a width of 15 ps. Inset: low intensity limit. The values are given in units of [molecules per pulse]$^{1/2} \times 10^3$. The highest value at this graph corresponds to a yield of 0.06 molecules per pulse.

wave function. Further increase of the intensity leads to saturation and even a decrease due to Rabi cycling of the excited-state amplitude back to the ground electronic state. This dependence seems to confirm the unitary PA mechanism as conjectured above. Nevertheless, as can be seen from the inset of the figure, for extremely low intensities the square root of the yield becomes linear with respect to the field. This suggests that the process is second order in the field intensity.

The three panels of Fig. 5 exhibit the bound-state population as a function of time following the dynamics. Three pulse widths are examined: 30 ps, 480 ps, and 2 ns. The terminal value of the population is the yield per pulse. The various lines represent several intensity values, as indicated in the panels' legends (in W/cm^2). It is clear that the yield saturates for short pulse durations (see the left panel). The solid blue line represents the intensity in which the pulse is able to remove all nonbound components from the scattering

wave function. At this intensity the system reaches the maximal total yield of 0.7 molecules per pulse. An increase of the intensity causes Rabi cycling accelerating the wave function toward larger internuclear separation, thus reducing the final yield.

Longer pulses allow more time for Rabi cycling, thereby reducing the yield. For pulse duration of 30 ps and the proper intensity, the maximal yield could be reached at the end of the pulse. For longer pulses the bound-state population reaches a maximum during the pulse, but decreases toward the end of the pulse, even for the optimal intensity. Monotonic increase of the bound-state population could be obtained for lower intensities, but the yield becomes suboptimal. Apparently, for short pulse duration the pulse can distill the stationary wave function from its nonbound components. The internuclear dynamics starts to intervene in the photoassociation for longer pulses. As can be seen in the right panel of Fig. 5, the system's dynamics is not necessarily destructive and a revival of the PA yield could appear for higher intensities.

Finally, the approach to the cw photoassociation limit is studied in Fig. 6. It is expected that in the cw limit the unitary PA should approach zero. Under such conditions the Fermi golden rule enforces an energy conservation constraint, restricting transitions to states with different energy. The insight gained from the study of transform-limited pulses is an input for further optimization based on coherent control.

IV. LOCAL CONTROL

Improving the yield beyond the transform-limited pulse requires the use of coherent control techniques. Local control theory is formulated in the time domain seeking at each instant the field that leads to the optimal rate of accumulation of the desired objective [20–23]. Local control theory has been applied to enhance the density at close distance as a launching point for photoassociation [24,25].

A. Formalism

Quantum coherent control methods use quantum matter interferences to optimize an objective [26–29]. Within the
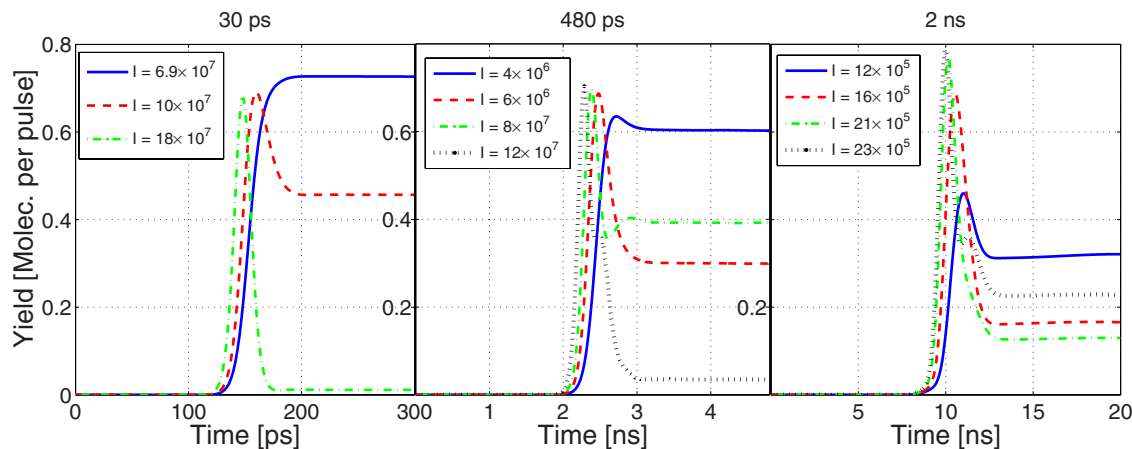
FIG. 5. (Color online) Dynamics of the PA induced by transform-limited pulses. Population on the (last) bound vibration state as a function of time in units of molecules per pulse for three different pulse widths. The pulse widths are indicated on titles of the three panels. Peak intensities are in units of W/cm^2.
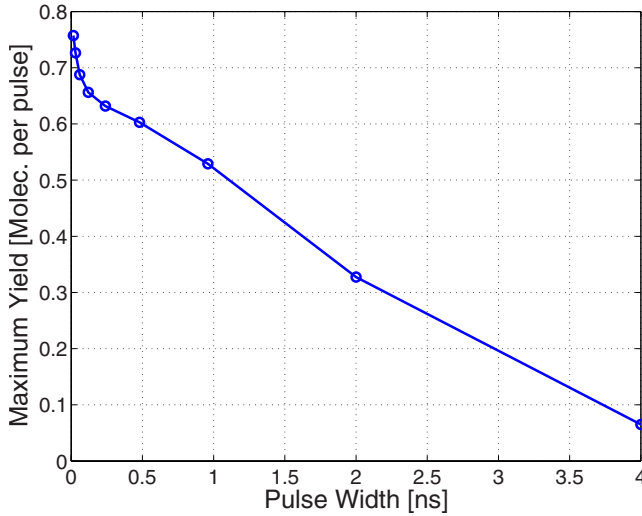
FIG. 6. (Color online) Maximal yield for PA under transform-limited pulses as a function of the pulse duration.

various methods that have been developed, local quantum control (LC) has the advantage that it can provide an interpretation to the mechanisms of the controlled processes [30]. The formalism is based on the Heisenberg equation of motion for the expectation value of the objective, defined by the operator $\hat{\mathbf{A}}$:

$$\frac{d\langle\hat{\mathbf{A}}\rangle}{dt} = -\frac{i}{\hbar}\langle[\hat{\mathbf{H}},\hat{\mathbf{A}}]\rangle. \qquad (9)$$

In the present case the objective is the projection on the bound states $\hat{\mathcal{P}}_g$, leading to

$$\frac{d\langle\hat{\mathcal{P}}_g\rangle}{dt} = \frac{2}{\hbar}\text{Im}[\langle\psi_g|\phi\rangle\langle\phi|\mu|\psi_e\rangle\epsilon(t)]. \qquad (10)$$

It is convenient to characterize the scalar products between the target bound wave function and other functions by an amplitude and phase representation

$$\langle\psi_g|\phi\rangle = p_g\exp(i\varphi_g),$$

$$\langle\psi_e|\phi\rangle = p_e\exp(i\varphi_e),$$

$$\langle\psi_e|\hat{\mathbf{V}}_d|\phi\rangle = p_d\exp(i\varphi_d). \qquad (11)$$

The amplitudes p_i are real non-negative numbers. $\hat{\mathbf{V}}_d \equiv \hat{\mathbf{V}}_g - \hat{\mathbf{V}}_e$ is the difference potential. In addition, the field is also described using amplitude and phase

$$\epsilon(t) = |\epsilon(t)|\exp(i\varphi_\epsilon). \qquad (12)$$

Inserting the operator $\hat{\mathcal{P}}_g$ [see Eqs. (3) and (4)] into Eq. (9) leads to

$$\frac{dp_g}{dt} = \frac{2}{\hbar}\mu p_e|\epsilon|\sin(\varphi_g - \varphi_e + \varphi_\epsilon). \qquad (13)$$

The bound-state population is hence controlled by the intensity of the field, the magnitude of the projection of the

excited-state wave function on the bound state, and three phase factors for the field and the ground- and excited-state projections. A similar treatment for the change in time of the projection of the target bound state on the excited state $\mathcal{P}_e = |\phi\rangle\langle\phi|\otimes|e\rangle\langle e|$ leads to

$$\frac{dp_e}{dt} = \frac{2}{\hbar}[p_d\sin(\varphi_g - \varphi_e + \varphi_d) - \mu p_g|\epsilon|\sin(\varphi_g - \varphi_e + \varphi_\epsilon)]. \qquad (14)$$

Comparison between Eqs. (13) and (14) shows that the ground- and excited-state projections are controlled by the same phase factors. As a result, it is impossible to control these two entities independently. Note further that the excited-state projection depends also on a field-independent component which arises from the fact that the target bound state is not an eigenstate of the excited-state Hamiltonian $\hat{\mathbf{H}}_e = \hat{\mathbf{P}}^2/2m + \hat{\mathbf{V}}_e$, and hence $[\hat{\mathbf{H}}_e, \hat{\mathcal{P}}_g] \neq 0$.

B. Implementation

1. Short time scales

The implementation of the control scheme depends on a global envelope function defining the duration of the process. Maximizing the target ground-state population accumulation sets the phase of the field to $\varphi_\epsilon = \pi/2 - \varphi_g + \varphi_e$, so that for all times $\frac{dp_g}{dt} = 2/\hbar p_e\mu|\epsilon| \geq 0$. As a result p_g is guaranteed to rise monotonically. To improve the control performance and to avoid rapid variations of the phase that results from the control, it was found advantageous to take the field to be proportional to p_e [31,32]

$$\epsilon(t) = |\bar{\epsilon}(t)|p_e\exp[i(\pi/2 - \varphi_g + \varphi_e)], \qquad (15)$$

where $|\bar{\epsilon}(t)|$ is the slowly varying Gaussian envelope of the field. Note that due to the form of the controlled field, the peak intensity of the envelope and the actual peak of the pulse do not necessarily coincide. Physically, the extra constraint of Eq. (15) tends to concentrate the applied field at instants of time where it is effective.

The main frame of Fig. 7 presents the bound-state population as a function of time for a pulse width of 15 ps. For comparison, the yield for a transform-limited pulse corresponding to the saturation intensity ($I = 1.6 \times 10^8$ W/cm^2 at the peak) is shown as a solid blue line. Two examples for dynamics under locally phase-controlled fields are presented in dashed black and dot-dashed lines. The peak intensity of the envelope of the dashed black line is taken *a priori* to be higher than the dot-dashed red line. The two insets present the real and imaginary parts of the field used for the three cases. As can be seen from the figures, the yield for all cases is practically identical. The optimal pulses from local control are very similar to transform-limited pulses.

The local control solution uses a more intense field to increase the bound-state population at earlier times with the elimination of the Rabi cycling at later times. A different view of the control field can be obtained by viewing the Wigner transform of the pulses. Figure 8 presents the contour plots of the Wigner function which corresponds to the three
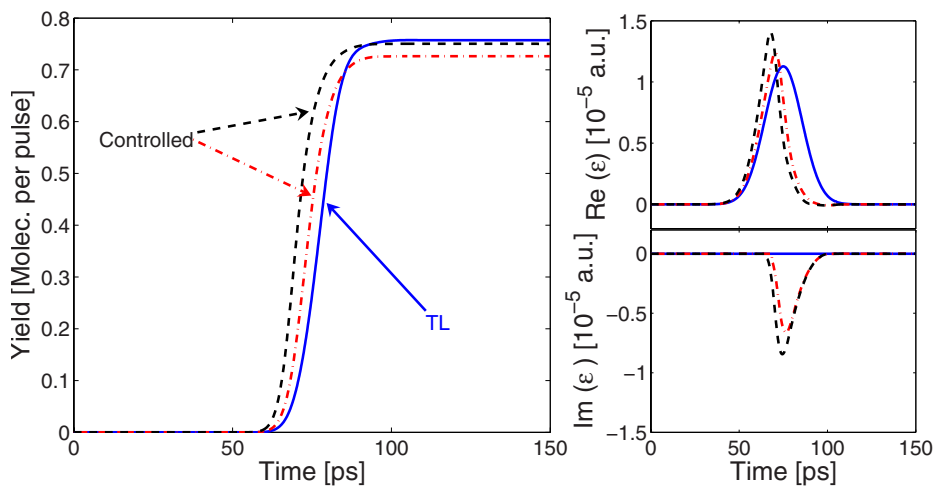
FIG. 7. (Color online) Controlled vs transform-limited pulses PA for short pulse widths. Main frame: bound-state population as a function of time for a transform-limited pulse (solid blue line) and two controlled pulses (dashed black and dot-dashed red lines). The two controlled pulses differed by the preprogrammed peak intensities. Note that the actual peak intensity may vary according to Eq. (15). Upper and lower insets: the real and imaginary parts of the field corresponding to the yields in the left panel.

pulses of Fig. 7. The control pulses begin as transform-limited pulses and end up with a linear chirp of the order of 3 GHz/ps. The role of this chirp is to eliminate Rabi cycling [33].

From these results it becomes evident that for pulse widths that are short or comparable to the time scales of the system's spatial dynamics—e.g., a few tens of ps in the case of Rb_2—the maximum yield for generating bound states is determined by the initial stationary scattering state. Transform-limited pulses with the proper intensity and width have the same performance as the optimized pulses.

2. Long time scales

For longer pulse duration a different scenario emerges. Figure 9 presents the bound-state population as a function of time for a pulse width of 2 ns. The dashed blue line represents the transform-limited pulse with peak intensity of 16 $\times 10^5$ W/cm². The black line is the controlled pulse. The controlled pulse maintains the monotonic rise of the bound-state population and approaches a yield which is very close to the impulsive PA limit, (see Figs. 5 and 7). It seems that for these time scales, the control strategy does not exploit the dynamics of the system. The reason can be seen at the inset of Fig. 9. Before any excited-state dynamics can develop, the pulse moves population to the bound state [see Eqs. (13) and (14)]. A control that transforms the maximum amplitude into p_g directly exhausts the amplitude p_e. With the current con-

trol strategy this maximization assures a monotonic increase of the bound-state population on the ground state, but cancels out the possibility of any free molecular dynamics that will contribute at later times to the photoassociation event.

A solution for this difficulty is to maintain a monotonic increase of p_g and avoid the complete depletion of the projection p_e on the excited state. This strategy will allow one to correlate the variation of the pulse phase to the system's dynamics. This task could be achieved by defining the field as

$$\epsilon(t) = |\bar{\epsilon}(t)| p_e \exp[i(\eta \pi/2 - \varphi_g + \varphi_e)], \qquad (16)$$

where $0 \leq \eta \leq 1$ is a balance parameter which controls the excited-state projection. Large values of η will induce sudden changes in the pulse, while smaller values will follow the system's dynamics adiabatically.

Figure 10 follows the temporal bound-state population for several values of η. For $\eta = 0.04$ the bound-state population increases steadily, reaching a final yield of five molecules per pulse. This yield is almost an order of magnitude larger than the impulsive limit of the PA. It seems that under these conditions the pulse follows the system's dynamics and adiabaticity is conserved. For smaller values of η the system's dynamics is faster than the response of the field and control fails. A further increase of the pulse width to 4 ns increases
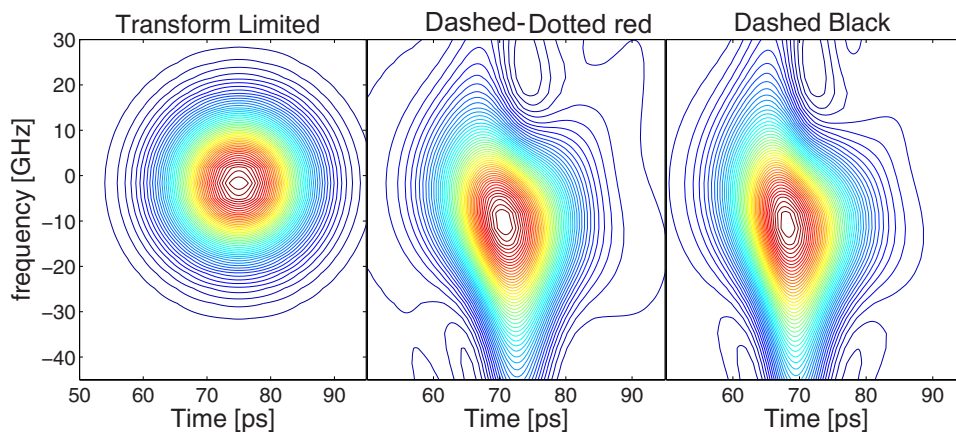
FIG. 8. (Color online) Wigner plots (scaled intensity vs time and frequency) for the three pulses of the insets of Fig. 7. The various panels correspond to the lines according to the titles.
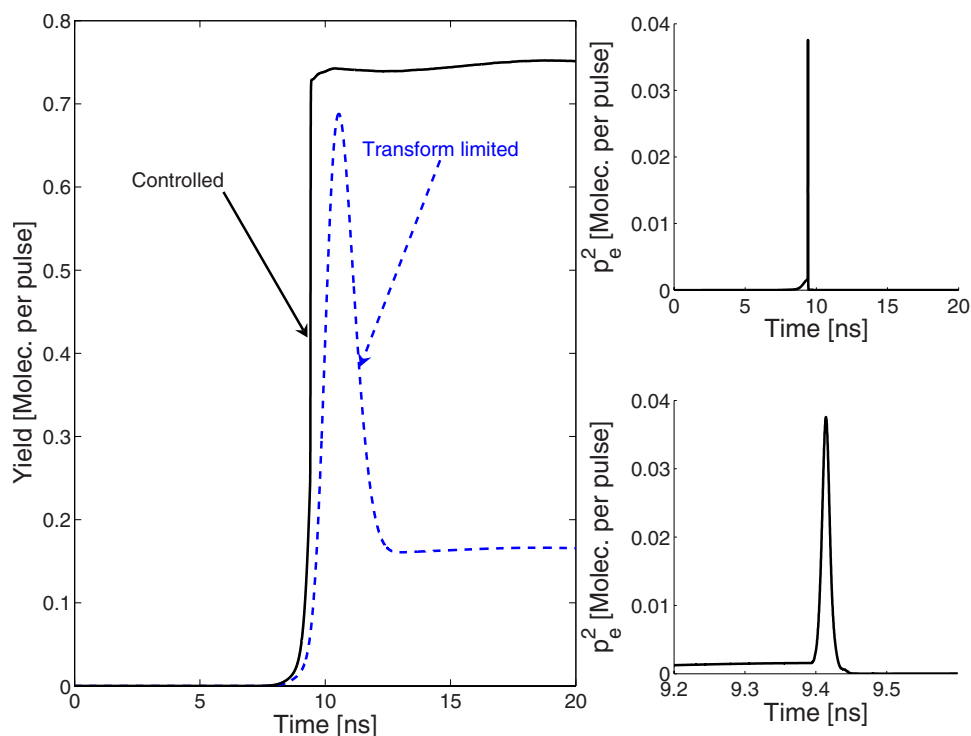
FIG. 9. (Color online) Control of the dynamical PA for long pulses. Main frame: bound-state population as a function of time. Blue dashed line: transform-limited pulse with a width of 2 ns and saturation peak intensity—i.e., maximal obtained yield. Solid black line: phase and amplitude-controlled pulse under the condition of Eq. (15). Upper inset: projection of the excited-state wave function onto the target bound state, p_e^2, as a function of time for a propagation under the controlled scheme. Lower inset: a blowup of the upper panel around the spike. The apparently discontinuous peak is a smooth peak with a width of $\sim$20 ps.

the yield even more, reaching 30 molecules per pulse (see the inset of Fig. 10).

Analysis of the optimal control fields was carried out using a sliding window Fourier transform (a direct Wigner transform for the highly featured pulse is infeasible computationally). Figure 11 exhibits a contour plot of the signal.
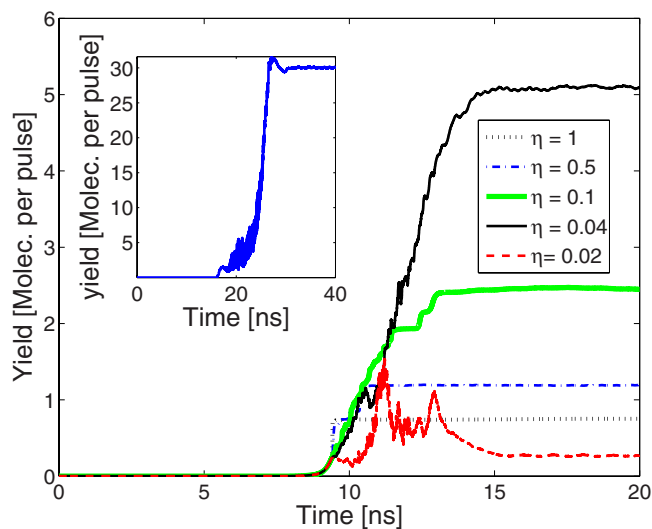
FIG. 10. (Color online) Adiabatic local control. Main frame: bound-state population as a function of time for various values of the balance parameter η [see Eq. (16)]. For comparison, the dotted black line shows the population under the control according to Eq. (15) where the impulsive PA limit is achieved. Rest of the lines: phase and amplitude-controlled pulse under the condition of Eq. (16). The values of η are denoted in the legend. The pulse width is 2 ns. Inset: same as the main frame for a width of 4 ns and $\eta = 0.04$.

The window's width for this analysis is 20 ps. Despite the complexity of the features, several features are worth noting.

(i) The pulse can be decomposed to a limited (seven here) set of major frequency components. These components are switched on and off and chirped.

(ii) The typical temporal width of a feature in the pulse is a few tens of picoseconds—that is, the time-scale of the system's dynamics (see the lower inset of Fig. 8).

(iii) Smearing of the components on the frequency axis may suggest a shaped field. This cannot be confirmed by the sliding window analysis which does not conserve the phase relations.
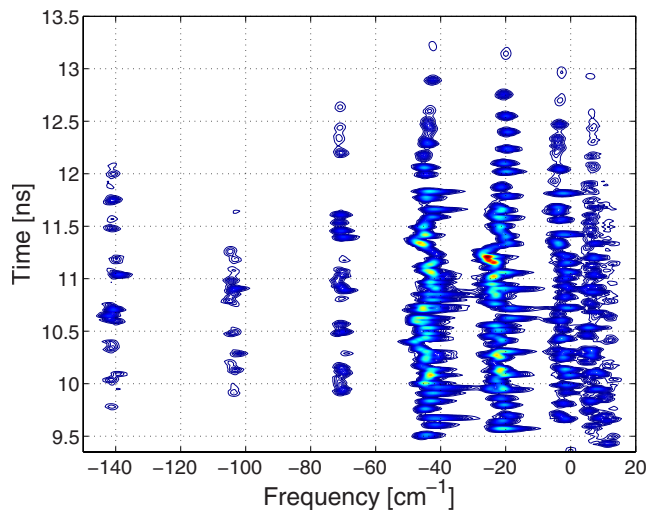
FIG. 11. (Color online) A sliding widow Fourier transform analysis for the $\eta = 0.04$ pulse of Fig. 10. The window width is 20 ps. A qualitatively similar picture is obtained for other widow widths.
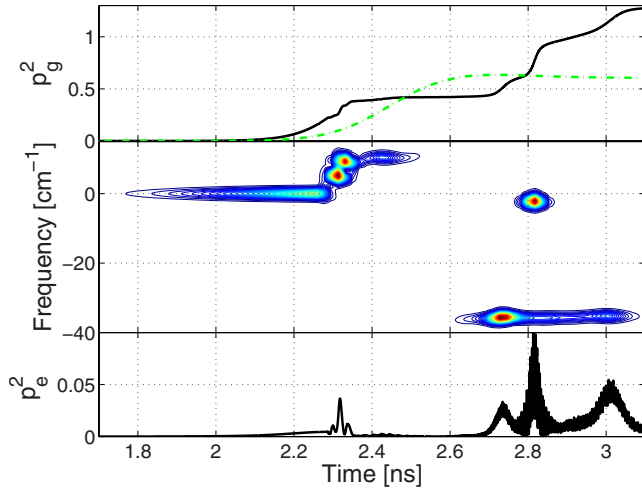
FIG. 12. (Color online) Control of the unitary PA for intermediate time scales. Upper panel: bound-state population vs time for the maximal possible yield under transform-limited pulse (dashed green line) and for the best adiabatically controlled scheme for η =0.2 (solid black line). Middle panel: the same as in Fig. 11 with the pulse used in the control of the upper panel. Lower panel: projection of the excited-state wave function onto the target state vs time for the controlled case (black line of the upper panel).

New developments of experimental techniques for pulse shaping at the nanosecond regime are under investigation [34]. The current feasible shaping frontiers cannot deal with the bandwidth and complexity of the current pulses suggested by the local control analysis. Nevertheless, assuming that such a pulse shaper would be available, it would seem that a self-learning algorithm aimed at optimizing the yield is expected to increase the PA yield beyond the impulsive PA yield by several orders of magnitude.

3. Intermediate time scales

The optimal time scales for quantum control of one pulse PA should match the dynamics typically in the order of a few hundreds of ps. Pulses with a temporal width of 480 ps are explored to complete the picture. The upper panel of Fig. 12 presents (as the dot-dashed green line) the time-dependent probability for the target bound state p_g^2 as a function of time for the highest achievable yield for transform-limited pulses. The yield is close to the impulsive PA limit. The solid black line compares the impulsive result to the adiabatically controlled scheme. The optimal η was found to be equal to 0.2 for these pulse widths, and the yield is twice the impulsive PA limit.

The middle panel of the figure exhibits a sliding windows analysis for the optimal pulse. The lower panel presents the projection of the excited state on the target bound state, p_e^2. At the beginning of the pulse one can see the transform-limited component at zero detuning. A slow growth of the ground- and excited-state projections is obtained in the early stage of the pulse. At the next step, two additional components with small blue detuning increase the projection on the excited state and deplete it slowly to the ground state. Note the similarity between the features of the pulse and p_e^2. After

the amplitude of p_e^2 vanishes, no bound state is produced. The system is then allowed to propagate freely for about 300 ps. A second couple of partially overlapping control pulses, now red detuned, are then applied for a second step of PA. The frequencies that appear on the control do not match any of the ground state. An interpretation for these frequencies will be given in the next section.

V. MECHANISM AND INTERPRETATION

The first explanation for the unitary photoassociation is a sudden elimination of amplitude from the scattering wave function at positions larger than the outer turning point of the bound state. This argument can justify some of the fundamental aspects of the effect such as the dependence of the PA yield on the detuning. However, this interpretation cannot account for the second-order dependence on the field intensity at the low intensity limit and the appearance of blue- and red-detuned sidebands in the spectrum of the local control pulses (see Fig. 12).

A more stringent analysis of the mechanism is obtained by inspecting in phase space the Wigner function generated from the product of the bound ground-state projection operator: $\mathcal{P}_g = |\phi\rangle\langle\phi|$ with the projection defined by the ground-state wave function $\mathcal{P}_{\psi_g} = |\psi_g(t)\rangle\langle\psi_g(t)|$ [35,36]:

$$\mathcal{W}_p(p,R) = \mathcal{W}_g(p,R)\mathcal{W}_{\psi_g}(p,R), \qquad (17)$$

where $\mathcal{W}(p,R) = \frac{1}{\pi\hbar}\int dy\ \psi^*(R-y)\psi(R+y)e^{i2py/\hbar}$. ψ is either the bound state ϕ or $\psi_g(R,t)$. $\mathcal{W}_p$ represents the phase-space overlap between the instantaneous ground-state wave function and the final target state. The upper left panel of Fig. 13 presents $\mathcal{W}_p$ at the initial time. Red and blue colors represent positive and negative values of the Wigner function. As could be expected, the Wigner function $\mathcal{W}_p$ is symmetric with respect to the momentum axis and the positive and negative components cancel out, meaning that the wave functions are orthogonal, $\iint\mathcal{W}_p(p,R)dp\ dR = 0$.

The phase-space Wigner function is first demonstrated on photoassociation with a very short pulse duration of 2 ps. The peak intensity of the pulse is the saturation intensity $I = 2.0 \times 10^9$ W/cm². For such a pulse, the impulsive limit is valid, meaning that the kinetic energy operator can be neglected. As a result, amplitude cannot flow from one position to another during the pulse. The upper right panel of the figure shows $\mathcal{W}_p$ corresponding to a pulse with the optimal blue detuning, $\Delta = 120$ GHz. Following the evolution of $\mathcal{W}_p$, the main change is the shift of amplitude from positive to negative momentum. This can be rationalized by a population transfer to the repulsive potential inducing a momentum kick. As a result, the balance between the negative and positive regions of $\mathcal{W}_p$ is distorted. This leads to the interpretation that the real impulsive unitary mechanism of generating bound states is induced by a momentum kick.

A change of the detuning will promote amplitude from different internuclear distances to the repulsive potential. The left lower panel of the figure displays the $\mathcal{W}_p$ function for a red-detuned pulse. Under these conditions the whole dressed excited-state potential lies entirely above the ground-state
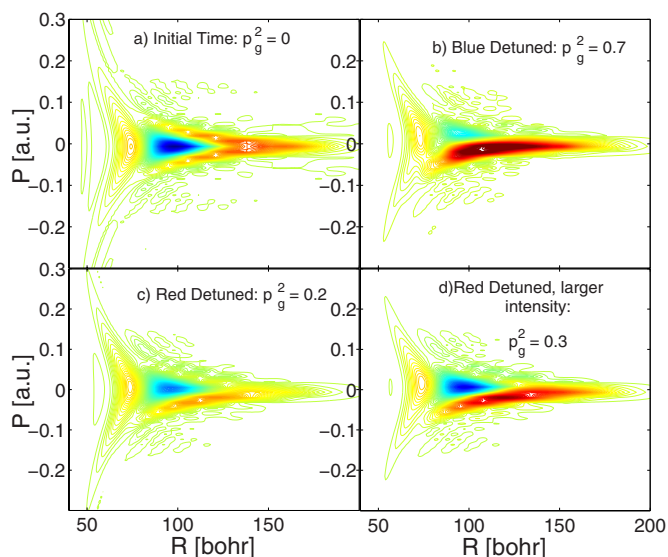
FIG. 13. (Color online) Mechanism of the unitary PA, the Wigner function $\mathcal{W}_p(P,R)$ representing the product of the target wave function with the excited-state wave function. The color coding is red for positive and blue for negative values. Upper left panel: initial conditions. Overlap with the initial scattering state $|\psi_g(t=0)\rangle$. Upper right panel: $|\psi_g\rangle$ is the wave function subsequent to the saturation transform-limited pulse with pulse width of 2 ps. The peak intensity is $I=2.0\times10^9$ W/cm². The detuning is $\Delta=120$ GHz. Lower left panel: same as panel (b) now with red-detuned light $\Delta=-70$ GHz. Lower right panel: same as panel (c) with $I=3.0\times10^9$ W/cm². The PA yield for each of the cases is given in units of molecules per pulse.

potential. This means that no internuclear distance is on resonance. As a result, population transfer to the excited state after the pulse is oversuppressed. Nevertheless, during the pulse a transient is created where a force leads to an acceleration and momentum increase. This is the mechanism of impulsive stimulated Raman scattering (ISRS) [37]. For this process the momentum gain is estimated as $\delta P\approx\frac{\mu^2\epsilon^2\tau}{\Delta^2}\left\langle\frac{\partial\hat{V}_d}{\partial R}\right\rangle$. As can be seen, this effect distorts slightly the symmetry of $\mathcal{W}_p$ and causes a non-negligible PA yield even for red-detuned light. An increase of the amplitude of the transient is caused by a larger intensity. The right lower panel of the figure displays the Wigner function for a peak intensity of $I=3.0\times10^9$ W/cm². As can be seen, the ISRS effect is more pronounced and the PA efficiency increases accordingly. It should be remarked that for realistic calculations a red-detuned PA will encounter the attractive potential curves of the Rb_2 system. These potentials were omitted in the present demonstration.

The detuning of the pulse from the atomic line determines the region where the momentum changes. For the optimal detuning, $R_C\sim120$ bohrs, the center of the distortion is at the peak of the overlap phase-space function $\mathcal{W}_p$. As can be seen from the two lower panels of Fig. 13, a detuning toward red frequencies shifts the point R_C and the region of the momentum distortion to larger internuclear distances. A blue-detuned light causes a distortion at smaller R. This observation gives insight into the origin of the frequencies that appear in the optimized pulses described in Sec. IV B. The

control strategy adjusts the field to increase the projection onto the target state according to the instantaneous conditions. This process is carried out dynamically, and when amplitude arrives at a phase-space region which overlaps the target the pulse is adjusted accordingly.

The momentum acceleration mechanism is also consistent with the apparent second-order scaling of the yield with respect to the field for vanishing field intensities. At low field intensity, the rate determining step of the process is the ISRS. As a Raman type of process, ISRS process has a second-order dependence on the field intensity. For higher intensities, the rate of the process is determined by the quantum unitarity—i.e., the ability to transfer amplitude from the ground to the excited state. This process has a first-order character.

VI. SUMMARY AND CONCLUSIONS

Pulsed ultracold photoassociation is characterized by a minor fraction of free-atom pairs becoming bound and then detected as molecules. Efficient molecular detection can serve as an extremely accurate measurement for changes on the initial scattering state. This means that even a small yield of unitary photoassociation can be detected. As demonstrated in this paper, optimizing the excitation pulse can lead to significant molecular generation reaching the typical molecular rate of cw photoassociation.

The dynamical time scale of the ultracold unitary photoassociation was found to be associated with the acceleration on the excited-state potential. For the Rb_2 system this time scale is in the order of a few tens of picoseconds. Two mechanisms of unitary photoassociation have been identified.

(i) Impulsive PA—typical for pulses shorter or comparable to the system's phase dynamics. The PA maximal yield is determined by the stationary scattering state. This maximal yield is generated by transform-limited pulses. As a result, pulse shaping techniques have only a minor consequence.

(ii) Dynamical PA—typical for pulse durations comparable to the nuclear dynamics. For transform-limited pulses, a reduction of the total yield was observed. Coherent control is able to enhance the yield of the PA by orders of magnitude. A yield more than 50 times the impulsive PA limit for pulses of 4 ns was calculated. Currently, pulse-shaping techniques are not sufficient for the control task.

At this point it should be emphasized that the control scheme studied employed only the repulsive part of the excited-state potential. Additional control possibilities emerge if both attractive and repulsive excited-state potentials are employed simultaneously.

Finally, the present study can lead to insight into experimental possibilities on similar systems. Many experiments on the Rb_2 system are performed on ^{85}Rb which take advantage of its extremely large scattering length. The present simulations were performed on the ^{87}Rb system which has a smaller scattering length. A preliminary calculation for the ^{85}Rb system shows that the influence of the isotope is minor for the impulsive PA. This mechanism of PA is influenced primarily by the amount of sudden momentum change. This

rate is therefore determined by the excited-state potential which is identical for both isotopes. The dynamical PA was found to be dramatically enhanced by isotope substitution. A yield of 60 molecules per pulse, for a pulse width of 2 ns, was obtained, an order of magnitude higher than the yield of ^{87}Rb.

Typical pulsed PA experiments have a repetition rate of the order of $\sim$1 kHz. One might thus be concerned about the possibility of destructive photodissociation of molecules that were created in the previous pulse. Simulations show that the survival probability for molecules in the last bound vibrational level ranges between 20% and 40%. This means that it is desirable to follow the PA pulse by a stabilizing pulse which removes the population to a deeply bound vibrational state as shown in Ref. [15]. The survival rate of a molecule at any state below the last bound state was calculated and found to exceed 99.9%.

The unitary PA was shown to be generated by a removal of amplitude from the scattering state. The mechanism involves impulsive changes both in momentum and in position. In the low intensity limit the momentum generation dominates similar to the ISRS process. For higher pulse intensity the process is generated by the removal of amplitude from the ground state and thus it becomes first order and scales linearly with the field intensity.

[1] M. J. Jones, E. Tiesinga, P. D. Lett, and P. S. Julienne, Rev. Mod. Phys. **78**, 483 (2006).

[2] C. McKenzie, J. Hecker Denschlag, H. Häffner, A. Browaeys, L. E. E. de Araujo, F. K. Fatemi, K. M. Jones, J. E. Simsarian, D. Cho, A. Simoni *et al.*, Phys. Rev. Lett. **88**, 120403 (2002).

[3] H. R. Thorsheim, J. Weiner, and P. S. Julienne, Phys. Rev. Lett. **58**, 2420 (1987).

[4] A. Fioretti, D. Comparat, A. Crubellier, O. Dulieu, F. Masnou-Seeuws, and P. Pillet, Phys. Rev. Lett. **80**, 4402 (1998).

[5] M. J. Wright, S. D. Gensemer, J. Vala, R. Kosloff, and P. L. Gould, Phys. Rev. Lett. **95**, 063001 (2005).

[6] M. J. Wright, J. A. Pechkis, J. L. Carini, S. Kallush, R. Kosloff, and P. L. Gould, Phys. Rev. A **75**, 051401(R) (2007).

[7] J. Vala, O. Dulieu, F. Masnou-Seeuws, P. Pillet, and R. Kosloff, Phys. Rev. A **63**, 013412 (2001).

[8] E. Luc-Koenig, R. Kosloff, F. Masnou-Seeuws, and M. Vatasescu, Phys. Rev. A **70**, 033414 (2004).

[9] Christiane P. Koch, F. Masnou-Seeuws, and R. Kosloff, Phys. Rev. Lett. **94**, 193001 (2005).

[10] C. P. Koch, R. Kosloff, and F. Masnou-Seeuws, Phys. Rev. A **73**, 043409 (2006).

[11] Ulrich Poschinger, Wenzel Salzmann, Roland Wester, Matthias Weidemüller, Christiane P. Koch,and Ronnie Kosloff, J. Phys. B **39**, S1001 (2006).

[12] Christiane P. Koch, Ronnie Kosloff, Eliane Luc-Koenig, Françoise Masnou-Seeuws, and Anne Crubellier, J. Phys. B **39**, S1017 (2006).

[13] B. L. Brown, A. J. Dicks, and I. A. Walmsley, Phys. Rev. Lett. **96**, 173002 (2006).

[14] W. Salzmann, U. Poschinger, R. Wester, M. Weidemüller, A. Merli, S. M. Weber, F. Sauer, M. Plewicki, F. Weise, A. Mirabal Esparza *et al.*, Phys. Rev. A **73**, 023414 (2006).

[15] C. P. Koch, J. P. Palao, R. Kosloff, and F. Masnou-Seeuws, Phys. Rev. A **70**, 013402 (2004).

[16] M. Marinescu and A. Dalgarno, Phys. Rev. A **52**, 311 (1995).

[17] R. Kosloff and D. Kosloff, J. Comput. Phys. **63**, 363 (1986).

[18] V. Kokooline, O. Dulieu, R. Kosloff, and F. Masnou-Seeuws, J. Chem. Phys. **110**, 9865 (1999).

[19] S. Kallush and R. Kosloff, Chem. Phys. Lett. **433**, 221 (2006).

[20] R. Kosloff, A. Dell Hammerich, and D. Tannor, Phys. Rev. Lett. **69**, 2172 (1992).

[21] F. L. Yip, D. A. Mazziotti, and H. Rabitz, J. Phys. Chem. **107**, 7264 (2003).

[22] S. Gräfe and V. Engel, Chem. Phys. **329**, 118 (2006).

[23] R. S. Judson and H. Rabitz, Phys. Rev. Lett. **68**, 1500 (1992).

[24] S. Kallush and R. Kosloff, Phys. Rev. A **76**, 053408 (2007).

[25] E. Luc-Koenig, F. Masnou-Seeuws, and R. Kosloff, Phys. Rev. A **76**, 053415 (2007).

[26] D. Tannor, *Introduction to Quantum Mechanics: a Time Dependent Prespective* (University Science Books, New York, NY, 2006).

[27] D. J. Tannor, R. Kosloff, and S. Rice, J. Chem. Phys. **85**, 5805 (1986).

[28] P. W. Brumer and M. Shapiro, *Principles of the Quantum Control of Molecular Processes* (Wiley-Interscience, Hoboken, NJ, 2003).

[29] S. A. Rice and M. Zhao, *Optical Control of Molecular Dynamics* (Wiley, New York, NY, 2000).

[30] A. Bartana, R. Kosloff, and D. J. Tannor, J. Chem. Phys. **99**, 196 (1993).

[31] P. Marquetand, C. Meier, and V. Engel, J. Chem. Phys. **123**, 204320 (2005).

[32] P. Marquetand and V. Engel, J. Chem. Phys. **127**, 084115 (2007).

[33] J. Vala and R. Kosloff, Opt. Express **8**, 238 (2001).

[34] C. E. Rogers III, M. J. Wright, J. L. Carini, J. A. Pechkis, and P. L. Gould, J. Opt. Soc. Am. B **24**, 1249 (2007); C. E. Rogers, M. J. Wright, J. L. Carini, J. A. Pechkis, and P. L. Gould, *ibid.* **24**, 1500 (1992).

[35] S. Kallush, B. Segev, A. V. Sergeev, and E. J. Heller, J. Phys. Chem. A **106**, 6006 (2002).

[36] N. Zamstein, S. Kallush, and B. Segev, J. Chem. Phys. **123**, 074304 (2005).

[37] U. Banin, A. Bartana, S. Ruhman, and R. Kosloff, J. Chem. Phys. **101**, 8461 (1994).